3D Microstructural Characterization of Ni/YSZ Electrodes Exposed to 1 Year of Electrolysis Testing

Trini, Martina; Jørgensen, Peter Stanley; Hauch, Anne; Bentzen, Janet Jonna; Hendriksen, Peter Vang; Chen, Ming

3D Microstructural Characterization of Ni/YSZ Electrodes Exposed to 1 Year of Electrolysis Testing

M. Trini[a,z], P. S. Jørgensen[a], A. Hauch[a], J. J. Bentzen[a], P. V. Hendriksen[a], M. Chen[a,z]

[a] Department of Energy Conversion and Storage, Technical University of Denmark,
Frederiksborgvej 399, 4000 Roskilde, Denmark
[z] Corresponding Author E-mail Address: mtri@dtu.dk, minc@dtu.dk

Abstract

Long-term operation strongly affects the microstructure of Ni/YSZ cermets used in state of the art fuel electrodes for solid oxide cells. The microstructural changes are considered to heavily affect the cell degradation. In this paper, the characterization of the Ni/YSZ electrode of a solid oxide electrolysis cell tested as part of a stack tested for 1 year was performed through focused ion beam-scanning electron microscopy and energy dispersive X-ray spectroscopy. A reference cell and two locations of interest in the tested cell were selected: one at the steam inlet side and the other at the outlet. Considerable microstructural changes were observed in the tested cell compared to the reference cell and between the inlet and outlet side. A decrease in Ni (from 30 % in the reference cell to 24 % in the tested cell), and in percolating triple phase boundaries length (from 2.83 $\mu m/\mu m^3$ in the reference cell to 0.76 $\mu m/\mu m^3$ in the tested cell) was observed in the active fuel electrode. Based on the results of this work and previous studies we hypothesize that the degradation trend between different operating conditions at the inlet and outlet of the cell is related to the current redistribution inside the cell.

Introduction

The increased share of intermittent renewable energy in future green energy scenario raises the need for managing the energy production/energy demand mismatch. In this regard, developing effective means of converting and storing the electrical energy surplus generated by overproduction peaks is crucial for overall system economy and security of supply. The role of devices capable of efficiently converting electrical energy into a storable medium (e.g. hydrogen or carbon-based synthetic fuels) are become important in this context. For this purpose, solid oxide cells (SOCs) represent an interesting technology [1,2] since the same cell can be operated either in fuel cell mode as a solid oxide fuel cell (SOFC) or in electrolysis mode as a solid oxide electrolysis cell (SOEC) [3]. This characteristic makes it possible to use the same device for both electrical energy production and storage depending on the specific need.

Operational life spans of several years are required to make SOCs systems economically competitive on the market and long-term stability has to be guaranteed [4-8]. Hence, the systems, stacks, and cells and their individual components (such as manifolds, interconnects, electrodes etc.) must be reliable, robust and durable [3, 5]. Relating the specific cell operation conditions with the degradation processes of the cell material and microstructures has been the objective of many studies [8-18]. This field of research aims to ensure and improve the long-term durability of the individual cells in a stack. Microstructural changes have been seen to affect all the components inside the cells and are considered one of the main causes of performance degradation [3, 8, 11-18]. Furthermore, additional studies have been performed with the aim of relating the specific microstructure changes with the decrease in electrochemical performance [e.g. 7, 8, 11].

Several degradation mechanisms in SOECs have been proposed in the last years [3, 7, 8, 10, 11]. Specifically, several studies were performed to investigate the effects of temperature, gas composition and current density [7, 11-13]. In order to compare the microstructure of different cells, ideally several complementary characterization techniques have to be applied on the same sample to obtain a proper description of the specific phenomenon observed. Concerning the changes in the materials composition and microstructure, scanning electron microcopy (SEM) and energy dispersive X-ray spectroscopy (EDS) are useful techniques [3]. To obtain a full microstructural characterization of the electrode structures, focused ion beam-scanning electron

56   microscopy (FIB-SEM) technique has been extensively used [19-25]. The microstructural details that can be

57   extracted from 3D tomographic reconstructions such as particles size distribution [26] and triple phase

58   boundary (TPB) length [19-21, 25] provide quantification of microstructural features of the complex cermet

59   structure. These parameters can complement and support the interpretation of electrochemical performance

60   and durability data. Combining complete microstructural and electrochemical characterization can enable the

61   description and quantification of specific degradation mechanisms occurring in the cell.

62   An attempt to relate electrochemical and microstructural degradation in SOECs was made by Hauch et al. [8]

63   on cells tested for more than 1500 hours. It emerged that the Ni/YSZ electrode was the main source of

64   performance degradation and Ni coarsening was one of the main mechanisms contributing to the decrease of

65   active TPB sites for electrochemical reactions [27]. A qualitative post-mortem analysis was performed by Chen

66   et al. [11] on SOECs tested up to 1500 hours, the authors showed the influence of temperature and current

67   density on the Ni/YSZ electrode microstructure. It was observed that higher temperature and current density

68   cause significant loss in percolation in the active fuel electrode. Recently, a microstructural investigation on

69   long-term (i.e. 1000 hours) tested SOEC was reported by Hauch et al. [8]. By combining SEM and

70   electrochemical impedance spectroscopy (EIS) measurements, the authors proposed an optimized fuel

71   electrode microstructure capable of tolerating high $p(H_2O)$ and current density with a low enough fuel electrode

72   overpotential to make the SOC last for more than 5 years potentially. Few studies have investigated

73   microstructural characterization of SOEC tested for longer than a few thousands hours. Tietz et al. [10] carried

74   out a qualitative metallographic analysis of a 9000 hours tested SOEC by means of SEM images. For that

75   specific cell, the main microstructural degradation was observed in the electrolyte while the Ni-YSZ electrode

76   did not seem to be significantly affected by operation. In this context, a systematic quantification based on 3D

77   tomographic reconstructions of SOECs tested for several thousands of hours is missing.

78   Among several degradation mechanisms observed in Ni-YSZ electrodes Ni agglomeration and coarsening is

79   considered one of the main causes of performance loss for solid oxide cells [13, 28]. Many studies have been

80   focusing on the Ni coarsening effect in the last years and it has been found that the particles growth is faster

81   during the first hours (0-1000 h) of the test [13]. Much attention has been paid to microstructural changes in

82   the Ni phase, indeed, and at typical cell operating conditions, the YSZ can be considered a stable scaffold

83   wherein Ni re-distributes and increases in particles size. Tanasini et al. [28] observed this behavior through the

84   analysis of SEM images. To the best of the authors´ knowledge, only few studies addressed quantitative

85   microstructural characterization of Ni/YSZ electrode of SOEC tested as part of a stack [7, 29, 30] and a

86   quantitative assessment of Ni coarsening for several thousands of hours of operation under technologically

87   relevant conditions is still missing up to now.

88   In addition, only few examples of microstructural characterization of cells tested as part of a long-term tested

89   SOC stack can be found in the literature. Faes et al. [13] tested several stacks for a maximum of 1900 hours in

90   fuel cell mode and characterized the microstructure of Ni/YSZ electrodes by means of SEM micrographs.

91   Rinaldi et al. [30] tested a short SOEC stack for 10,700 hours and then analyzed the microstructural degradation

92   of each layer, the nickel depletion in the innermost region of the active fuel electrode was observed. Brisse et

93   al. [31] tested the cell characterized in this work as part of a stack for ~ 9000 hours in technologically relevant

94   operating conditions at the European Institute for Energy Research (EIfER). A preliminary microstructural

95   characterization of the same cell was reported by our group [29] with the aim of investigating the

96   microstructural degradation and we highlighted the differences between 2D and 3D quantification of the same

97   electrode microstructure.

98   Quantifying microstructural changes of SOC is important for understanding the degradation processes

99   occurring at the micrometer scale. With the aim of providing a detailed characterization of the microstructure;

100 we combine here 3D tomographic reconstructions with EDS. The 3D characterization performed on FIB-SEM

101 data provides detailed information on the network properties defining, not only the particles size, but also the

102 quality of the connections. However, only small volumes can be analyzed with this technique and, in this

103 regard, EDS maps provide important additional information of large areas of the cell. Two locations exposed

104 to different local operating conditions (i.e. gas composition, current density, and temperature) inside the same

105 cell were chosen for analysis: at the steam inlet and outlet. The microstructures of the two regions analyzed

106 were compared with a reference cell exposed to reduction only and no long-term operation. Ni re-distribution

107 was detected and changes in TPB and surface area of the three phases (i.e. Ni, YSZ and pores) were quantified.

108 Moreover, hypotheses are proposed to explain the difference observed between the two locations in the long-

109 term tested cell (inlet and outlet).

110 **Experimental**

111 One of 25 identical SOEC cells from a stack produced by Topsoe Fuel Cell A/S (Cell number 17 counting

112 from top of the stack) is analyzed in the present work. The cells have a Ni/3YSZ support ($\sim$ 300 µm thickness)

113 and a Ni/8YSZ fuel electrode ($\sim$ 15 µm thickness), a 8YSZ electrolyte, a CGO ($Ce_{1-x}Gd_xO_{2-x/2}$) barrier layer,

114 and a CGO/LSCF ($(La,Sr)(Co,Fe)O_{3-\delta}$) oxygen electrode. On the top of the oxygen electrode a current collector

115 layer is applied. The cells have an active area of 87.7 cm^2 and are stacked in between coated Crofer

116 interconnects [31].

117 <u>Testing and sample preparation</u>

118 The long-term electrolysis testing of the stack analyzed in this work was performed at the EIFER. Essential

119 parameters used for the operation are summarized in Table 1. Additional details about the test and stack

120 performance can be found elsewhere [31]. The reference cell used in this work was a cell from the same

121 production batch of the 25 cells in the stack. The reference cell was reduced at 750°C for 4 hours in moisturized

122 10 % H_2 in N_2 (10 % H_2, 90 % N_2) and not tested further. The Ni/YSZ electrode of the reference cell was

123 utilized for comparison with the tested cell.

124 <u>3D Characterization</u>

125 After the test, part of the stack (Cells 11-25) was embedded in epoxy resin and then sectioned for further

126 analysis. A sketch of the stack top view with relative sectioning is shown in Figure 1 a). A Zeiss XB1540

127 Crossbeam microscope was used for data collection by FIB serial sectioning on the reference cell and the two

128 locations of interest on the long-term tested cell: the fuel inlet and outlet side. For the sake of simplicity, the

129 three locations investigated will henceforth be defined as reference, inlet, and outlet, respectively. Cross

130 sections of the same cell were analyzed in a previous work [29] to compare 1D and 3D microstructural

131 characterization and to quantify degradation between the reference and the tested cell at the micrometer scale.

132 Three-dimensional characterization was previously performed only for the reference and the inlet part of the

133   tested cell [29]. Here, a more complete view of the aged cell is presented by adding the outlet dataset.

134   Furthermore, EDS analysis was performed on the regions of interest to estimate the chemical composition in

135   different locations of the cells. The regions used for FIB-SEM characterization and EDS analysis are illustrated

136   in Figure 1 b) and c) on the top of a SEM image of the reference cell showing the Ni/YSZ electrode and part

137   of the YSZ electrolyte. The yellow box in Figure 1 b) highlights the innermost 8 µm of the active fuel electrode

138   extracted from FIB-SEM dataset and used for the computation of microstructural parameters. Figure 1 c)

139   illustrates the areas used for acquiring EDS data, smaller areas of 25 x 3 µm^2 and 25 x 10 µm^2 were also used

140   for the fuel electrode and support layer, respectively. Figure 1d) shows a schematic drawing of the electrolyte

141   (~ 5 µm), the active fuel electrode (~ 15 µm), and part of the support layer (overall thickness ~ 300 µm) defined

142   with dashed lines since only partially interested by the analysis. The direction of the FIB milling front is

143   illustrated in Figure 1d together with the direction and width of the line scan recorded for the EDS analysis.

144   Due to slightly different microscope set-ups for the three samples analyzed, three different voxel sizes were

145   obtained: 25 x 25 x 40.80 nm^3 for the reference, 25 x 25 x 35.60 nm^3 at the inlet and 25.53 x 25.53 x 37.79

146   nm^3 at the outlet of the tested cell. In order to analyze the same volume size (approximately 12.5 x 8 x 20 µm^3)

147   in each sample, three sub-volumes were selected: 501 x 321 x 490 pixels for the reference cell, 501 x 321 x

148   564 pixels for the inlet and 491 x 314 x 531 pixels for the outlet. With the aim of analyzing the innermost part

149   of the active fuel electrode the dataset used for the computation of microstructural parameters starts, for each

150   volume, ~ 3 µm away from the electrode-electrolyte interface and extends ~ 8 µm towards the support layer.

151   The FIB milling front along the electrolyte is perpendicular to the electrode-electrolyte interface [32] (Figure

152   1); ~ 35 nm are milled away, a picture of the support/electrode/electrolyte cross section is obtained, and next

153   another 35 nm is milled away, and so forth, effectively collecting pictures of the cross section moving in the

154   direction parallel to the electrode-electrolyte interface. Two sets of images (i.e. obtained from Inlens and SE2

155   detectors) were recorded for each sample and used for post-processing and segmentation as described

156   elsewhere [32].

157   Once the segmented volumes were obtained, several analyses were performed on the inner fuel electrode sub-

158   volumes in order to compare the microstructure of the three locations investigated. The phase fraction of each

159   phase in the region of interest was calculated by dividing the overall volume of a single phase by the total

160   volume analyzed. The continuous PSD was computed as described earlier [26, 29, 32]. This method consists

161   in evaluating, for each 2D section of the 3D reconstructions, the largest circle that fits the particle and extending

162   that circle to a 3D sphere. The continuous PSD distribution is obtained by calculating the distribution of the

163   largest spheres that can fit inside each part of the structure. Moreover, the total and percolating TPBs were also

164   determined [22]. For what concerns the percolating sites, not only their total amount was determined but also

165   the networking quality through the characteristic pathway diameter [32]. In addition, the tortuosity factor of

166   the Ni and pore phase along the three directions of the volumes was determined using the program TauFactor

167   [33].

168   <u>Energy Dispersive X-ray Spectroscopy (EDS)</u>

169   In addition to the 3D microstructural characterization, compositional information was obtained for the

170   locations of interest by EDS. A field emission gun scanning electron microscope (Carl Zeiss Supra 35)

171   equipped with an energy dispersive X-ray detector (Thermo Electron Corporation – NORAN System SIX) was

172   used for the investigation. The EDS analyses were performed both as X-ray mapping, wide line scans, and as

173   area analysis on polished carbon coated cross section surfaces. The applied acceleration voltage of 15 kV

174   resulted in an interaction volume of ~1 μm^3. Cell number 17 in the stack was analyzed in the region close to a

175   contact point between the cell and the interconnect. EDS data from 25 x 3 μm^2 and 50 x 3 μm^2 areas were

176   recorded with NSS software using Proza (Phi-Rho-Z) correction, the data were then used to calculate the Ni/(Zr

177   + Y) atom ratio close to the electrode-electrolyte interface. In a larger area of the support layer, EDS data from

178   25 x (3 to 10) μm^2 and 50 x (3 to 20) μm^2 areas were used to calculate the Ni/(Zr + Y) atomic ratios. The

179   regions used for the EDS analysis is illustrated if Figure 1 c). The counting statistic error for each measurement

180   was estimated to be less than 1 %. In addition, 50 μm wide EDS line scans (50 points per line) perpendicular

181   to the electrode-electrolyte interface were recorded for the three locations of interest (Figure 1). The

182   measurement of each line scan started 4-5 μm inside the electrolyte and extended into the support layer

183   covering an overall length of ~ 38 μm. Acquisition times of 75 seconds per spectrum was used for the line

184   scans obtaining ~ 30,000 nickel counts and a background of ~ 2,500 counts.

185

Results

<u>3D Volumes</u>

A 3D rendering of three sub-volumes extracted from the investigated geometries is shown in Figure 2. The dimension of each sub-domain is ~ 8 x 8 x 8 μm^3 and the three phases of interest are represented as follows: Ni particles are red, YSZ scaffold is gray and pores are transparent. Part of the electrolyte is also introduced in the 3D reconstructions of Figure 2. Qualitative microstructural changes in the Ni phase can be identified clearly between the reference and both locations analyzed for the tested cell by simple visual inspection of the three cubes in Figure 2. The results of the 3D microstructural characterization performed on the three regions are presented in further detail in Table 2.

The central 8 µm of the Ni/YSZ active electrode were analyzed starting ~ 3 µm away from the electrolyte-electrode interface and stopping ~ 1 µm before the interface between the active electrode and the support layer. Table 2 summarizes microstructural parameters quantified on each of the volumes investigated.

<u>Overall phase fractions of the fuel electrode:</u>

The first parameter discussed is the phase fraction. The results are shown in Table 2. The cell under analysis has been manufactured aiming for a Ni/YSZ volume ratio of 40/60 vol%, therefore the minimum theoretical pore phase fraction obtainable after NiO reduction will be ~ 22%. This in turn leads to an upper limit for Ni phase fraction of 31.2 %. The computed Ni phase fraction of 30% for the reference cell is in good alignment with manufacturing data. A decrease of overall Ni phase in the active fuel electrode to approximately 23 % in the inlet side of the tested cell was observed. Meanwhile, the porosity showed an increase from 25 % calculated for the reference cell to 29 % after the test, both at the inlet and at the outlet. While the percentage of YSZ at the inlet side is almost un-changed compared to that of the reference cell, an apparent decrease is observed at the outlet side. Such a decrease can be attributed to the uncertainty of the measurement itself, as it will be explained later. The general trend observed in the present study for the Ni phase fraction is in agreement with

209 [34]. Performing the quantification of microstructural parameters in the innermost 8 µm of the electrode

210 provides important information on the degradation of the active part of the fuel electrode. In the data analysis,

211 the volume between 3 and 11 µm from the electrolyte interface was used for deducing microstructural

212 characteristics from the reconstructions. It should be noted that besides the Ni depletion observed in this zone

213 (Table 2) an even stronger depletion is seen close to the electrolyte (Figure 3 a)), within the first three microns,

214 which is not included in values behind Table 2. Estimating accurate confidence intervals for parameters

215 calculated from 3D image data is notoriously challenging. It is worth mentioning that several sources of errors

216 can bias the results: local variations of the structure, representative volume size, a subjective segmentation

217 step, finite resolution, and the parameter estimation method itself [35 - 37]. This is compounded by different

218 parameters having very different sensitivity to each of these types of errors. The equipment used for recording

219 the data combined with the implemented post-processing procedure allowed analysis of volumes of 12.5 x 8 x

220 20 µm^3 for each sample. Considering the mean radius of Ni particles ~ 1.26 µm [29] for the cell analyzed in

221 the current work and using the definition of dimensionless length given by Harris et al. [36], the dimensionless

222 dimensions of the volumes analyzed are 9.92 x 6.35 x 15.87 in dimensionless units. Lombardo et al. [37]

223 performed a volume-dependence investigation for Ni/YSZ SOFC anodes that showed that a characteristic

224 dimensionless length of ~ 6 is required for computing reliably the properties of the YSZ phase. In the current

225 work, the relative small size of the volume obtained from FIB-SEM reconstructions is reflected in the

226 uncertainty intervals estimations reported in Table 2. The tortuosity factor is one of the parameters most

227 affected by the size of the volume analyzed in particular when the percolation factor is low; in line with this,

228 the uncertainty of this parameter is estimated to be quite high (ca. 20 % at the inlet side as reported in Table

229 2). The uncertainty intervals in Table 2 are estimated on the basis of experience in parameters computation on

230 the same types of samples and imaging technique [35]. However, the results for the YSZ phase can provide

231 information on the accuracy of the measurements since the structure of this phase can be treated as stable. It

232 was sintered at 1300 °C and is unaffected by cell operation at 750 °C. For example, there is a discrepancy in

233 the YSZ phase fraction observed between the three locations: 45 % $\pm$ 2.50 in the reference, 47 % $\pm$ 2.50 at the

234   inlet and 43 % ± 2.50 at the outlet. This measurement provides an estimate for the uncertainty level for the

235   calculated phase fractions.

236   <u>Interface areas and TPB length:</u>

237   The surface area of each phase and the interface area between phases are used for the evaluation of

238   microstructural changes occurring in the Ni/YSZ electrode due to the long-term operation of the cell. The

239   results are summarized in Table 2. The overall surface area of Ni is decreased from ~ 1.7 to ~ 0.9 $\mu m^2/\mu m^3$

240   after long-term operation. The interface areas of pore and YSZ with Ni show a reduction after the testing

241   reaching ~ 0.3 and ~ 0.7 $\mu m^2/\mu m^3$ at the inlet side, respectively. The results point out similar degradation at

242   inlet and outlet side of the same cell after 1 year of operation, though to different degrees.

243   It is well known that electrochemical reactions inside the cell occur at active TPB sites only and these sites

244   need to be part of a percolating TPB to be active. A percolated site is obtained when the three phases defining

245   the TPB each have a percolating path for the conducted species (i.e. electrons through Ni, oxygen ions through

246   YSZ and gas through pores). Table 2 shows the results obtained from the computation of the TPB in the

247   samples analyzed. The length of total and percolating TPB was obtained as the average of the length computed

248   in each of the six directions of the 3D geometry analyzed. Table 2 shows that also the percentage of active

249   sites decreases after the long-term test. While 86 % of the overall TPB length was percolating in the reference

250   cell, only 53 % was percolating at the inlet of the tested cell. A significant difference can be appreciated in the

251   loss of active TPB sites between inlet and outlet, where 62 % of the TPB is percolating at the outlet.

252   While similar nickel depletion in the active electrode can be detected at the inlet and outlet side of the cell, a

253   more pronounced TPB length decrease is observed at the inlet side when compared to the outlet. This effect is

254   presumably linked with an effect of the local polarization, which is much larger at the inlet compared to the

255   outlet (the total cell overpotential was estimated to be ~ 420 mV at the inlet and ~ 320 mV at the outlet)

256   resulting also in a higher local current density [38]. The same trend obtained in the cell analyzed in this study

257   was qualitatively observed in the ~ 700 hours tested cells in reference [39], where 2D low voltage SEM images

258   showed a lower percolation degree at the inlet side. Moreover, the higher steam content at the gas inlet side of

259   the cell could contribute to the higher degradation observed there. Pihlatie et al. [40] observed that the cell

260   conductivity decreases as the steam content increases. Indeed, high steam content in the fuel promotes the

261   formation of $Ni(OH)_2$ complex that facilitates nickel diffusion and particles growth. In addition to that, the

262   steam content and the local polarization of the electrode affect the local pO_2 in the electrode that in turn

263   influences the wettability of Ni on YSZ. Experimental evidence of the effect of oxygen activity on Ni/YSZ

264   interaction was presented by Jiao et al. [41] and a theoretical correlation between pO_2 and Ni contact angle on

265   YSZ was proposed. Different wettability properties of Ni/YSZ cermets were qualitatively observed in [8] and

266   [39] between the inlet and the outlet of the cell where both gas composition and current density assume

267   different values.

268   <u>Phase fractions as a function of distance from the electrolyte-fuel electrode interface:</u>

269   Figure 3 illustrates the phase fraction calculated on each slice of the segmented volume parallel to the

270   electrode-electrolyte interface (i.e. the distance between the two neighboring slices is between 35 nm and 40

271   nm). The overall length covered by this analysis is ~ 16 µm for each sample. In the graphs of Figure 3 the

272   electrolyte is located to the left. Two vertical-dashed black lines indicate the region used for the computation

273   of the other microstructural parameters reproduced in Table 2. This region starts ~ 3 µm away from the

274   electrode-electrolyte interface and ends approximately 1 µm before the support layer. Due to the irregular

275   structure, it is not easy to define precisely where the interface between the electrode and the electrolyte is

276   placed. Conventionally, we placed the interface where the first nickel particle is found when moving from the

277   electrolyte towards the electrode. As evident from Figure 3 a significant decrease of the Ni content in the active

278   area is observed after long-term operation at both the inlet and the outlet of the cell to more or less similar

279   extent. In the support, on the other hand, no such depletion is observed, the Ni content in each slice of the

280   support layer in the tested cell is not much different from the one in the reference cell. In consistency with the

281   finding on the Ni phase Figure 3 b) shows a slight increase in porosity in the active fuel electrode after 1 year

282   of cell operation, whereas the porosity in the support layer after the long-term operation is not significantly

283   different from the reference one. The content of the YSZ along the direction perpendicular to the electrode-

284   electrolyte interface is illustrated in Figure 3 c). It is evident as the YSZ fraction in the electrode does not

285   change on aging. Even though Ni migration can be qualitatively appreciated in Figure 3, the local 3D analysis

286   performed in this study does not allow the observation of whereto the Ni moves due to the intrinsic limitation

287   of the analyzed volume with FIB-SEM tomography. Among the factors that lead to uncertainty in the analysis,

288   it must be remembered that raw FIB-SEM data were recorded and segmented such that the focus was on the

289   inner active fuel electrode. This means that data away from this region (i.e. the support layer) are more likely

290   to be affected by artifacts occurring in the segmentation process of the whole volume.

291   Figure 4 shows the results of the EDS analysis. Based on 1 to 5 measurements at different places in each of

292   the samples of interest, the Ni/(Zr+Y) atomic ratio was computed on a region of the electrode close to the

293   electrolyte interface and on a larger area of the support layer. The results are illustrated in Figure 4 a). The

294   ratio shown in Figure 4 a) is an indication of the Ni content in the different areas of the electrode. The intrinsic

295   uncertainty of the characterization method and the inhomogeneity of the sample can affect the measurement

296   of the nickel content. In this regard, 9 measurements were performed in the active electrode and 4 EDS maps

297   were recorded for the large area analyzed in the support layer. In order to give an estimation of the inaccuracy

298   of the measures, the standard deviation was computed to be ~ 0.18 and ~ 0.07, respectively for the active

299   electrode and the support layer. A significant nickel depletion in the region of the active electrode closest to

300   the electrolyte is observed at both inlet and outlet of the tested cell. A Ni/(Zr+Y) atom ratio of approximately

301   ~ 1.7 was obtained for the reference cell while the value drops below 1 in both locations of the tested cell. This

302   indicates that the migration of nickel away from the interface between the Ni/YSZ electrode and the electrolyte

303   occurs to similar extents at the inlet and the outlet side of the cell. Interestingly, the Ni/(Zr+Y) atom ratio

304   computed on the large area of the support layer does not vary considerably in the regions analyzed and it varies

305   between 1.6 and 1.8 for the three samples as shown in Figure 4 a).

306   Line scans were recorded starting from the electrolyte toward the support layer and used as further evidence

307   of nickel depletion in the active fuel electrode. The results are summarized in Figure 4 b). The graph in Figure

308   4 b) shows three line scans for the three locations of interest (i.e. reference, inlet and outlet) and the theoretical

309   Ni/(Ni+Y+Zr) atomic ratio of ~ 67% resulting from the production process (dashed gray line). The black

310   dashed line points out the electrode-electrolyte interface. The line scan results are in agreement with what

311 observed in Figure 3 and Figure 4 a). A systematic decrease in Ni content in the 5 µm of the active fuel

312 electrode closest to the electrolyte is recorded after long-term operation while only small variations can be

313 appreciated in the support layer.

314 <u>Particle size distributions:</u>

315 When performing the microstructural characterization of SOC electrodes it is useful to define the particle sizes.

316 In this work, the continuous particle size distribution method [26] was applied to compute the results shown

317 in Figure 5. For what concerns Ni particles, it was observed that the average particle radius is subjected to a

318 shift from approximately 350 nm in the reference cell to ~ 600 nm in both locations analyzed on the long-term

319 tested cell. A shift towards larger pore sizes was observed at both analyzed locations of the tested cell compared

320 to the reference cell, the measured YSZ particle size distribution is unaffected by the long-term operation. This

321 observation is well in line with previous studies [8, 28, 29] and the trend observed for Ni particles agrees with

322 the analysis performed by Hauch et al. [34], where the mean intercept length principle was applied on 2D SEM

323 micrographs and an increase in Ni particle size from ~ 1.01 µm in the reference cell to ~ 1.26 µm in the tested

324 one was observed. These results are in line with the particles size distribution obtained from the analysis of 2D

325 SEM images of the same cell analyzed here, the increase of Ni particle size from ~ 1.03±0.02 µm in the

326 reference cell to ~ 1.39±0.03 µm at the inlet side of the tested cell was observed [29]. The testing conditions

327 used for the cells analyzed in [34] were different from the ones applied to the stack analyzed leading to different

328 values of the Ni particles radius. However, the trend is the same in both cases.

329 <u>Characteristic pathway diameter and Ni tortuosity:</u>

330 The concept of characteristic pathway diameter has been used in other studies [29, 32], however, there using

331 the term "critical pathway radius" instead. The characteristic pathway diameter is the diameter of the largest

332 sphere that can be squeezed through the network of the phase of interest. This idea is sketched in Figure 6

333 where percolating TPBs are highlighted and possible pathways of electrons in the Ni phase are drawn. The

334 characteristic pathway diameter is pointed out in Figure 6 by red arrows.

335 The characteristic pathway diameter is a measure to evaluate the quality of the pathway connections of the

336 different phases; i.e. the width of the "Nickel highway" for the electrons and similar for the gas phase in the

337 pores and oxide ions in the YSZ phase. This parameter is important for understanding the quality of the

338 pathways connecting the three phases throughout the electrode. If the percolation of TPB sites is guaranteed

339 by pathways characterized by a very narrow diameter (e.g. 20 nm), then impurities, carbon deposition or

340 similar situated at the TPB may more easily break the network connectivity and therefore reduce the degree of

341 electrode percolation in the overall cell performance. On the other hand, if the pathway is characterized by a

342 larger characteristic diameter (e.g. 200 nm or above), the structure is more robust and impurities are less likely

343 to obstruct the connectivity. A significant change of the characteristic pathway diameter for the Ni phase can

344 be observed in Figure 7 a). Assuming for instance that a high performing cell is characterized by Ni connected

345 through pathways with a diameter around 200 nm, the percentage of paths with this characteristic is higher

346 than 80 % in the reference cell and is below 50 % at both the inlet and the outlet side of the tested cell. After

347 testing, the pores are connected through bigger paths as illustrated in Figure 7 b) whereas YSZ does not show

348 appreciable changes with respect to characteristic pathway diameter (Figure 7 c)).

349 The results illustrated in Figure 7 confirm the degradation trend observed in Figure 5: the characteristic

350 diameters of percolated pathways are degraded significantly to a similar degree for both the inlet and outlet

351 part of the cell after one year of testing.

352 The results in Table 2 show lower values of percolating TPB at the inlet side while the graphs presented in

353 Figure 7 report lower nickel percolation at the outlet. This effect could be due to the fact that the percolating

354 TPB length is computed by checking the percolation through all the three phases. Instead, the characteristic

355 pathway diameter shown in Figure 7 consider the individual percolation of each phase separately. One more

356 parameter that can be used as indication of networking quality is the tortuosity factor. This parameter was

357 computed using the TauFactor program [33]. The results are reported in Table 2, for Ni and pore phases of the

358 active fuel electrode. Increased tortuosity of the Ni networking and therefore pronounced degradation can be

359 appreciated when comparing the tested cell with the reference, although a clear difference between inlet and

360   outlet cannot be detected. The tortuosity factor computed on the pore phase reveals reduced tortuosity in the

361   tested cell compared to the reference.

Discussion

363   The locations investigated in this study were exposed to different local conditions: gas compositions, current

364   densities and temperatures inside the tested cell. The results presented here on phase fraction (Table 2) and Ni

365   migration (Figure 3) are in agreement with Mogensen et al. [39] where a study of Ni migration correlated with

366   current load is reported for SOFC and SOEC. In electrolysis mode, a loss of Ni in the innermost active fuel

367   electrode was observed [39]. A qualitative comparison between inlet and outlet based on 2D SEM images after

368   ~ 700 hours of testing is reported in reference [39] showing appreciable bigger Ni particle size and higher

369   percolation loss at the inlet than at the outlet side. The results for Pore/Ni and YSZ/Ni interface area

370   summarized in Table 2 show a decrease of approximately 69 % and 29 %, respectively, when comparing the

371   inlet side of the tested cell with the reference cell. The difference in the extend of the decrease can be related

372   to the inhibiting effect of YSZ on Ni coarsening as discussed in [40, 42]. Huber et al. [42] observed that the

373   morphological variation of nickel during the coarsening process is more pronounced on the Ni surface in

374   contact with the gas phase than at the YSZ/Ni interface. Indeed, the energy related to the Pore/Ni interface is

375   lower than the energy related to the adhesion of Ni on YSZ. This results in the smaller decrease of YSZ/Ni

376   interface area when compared to the decrease of Pore/Ni interface area (Table 2). The Ni rearrangements

377   observed in the cell investigated in this work are well in line with the observations of Hubert et al. [42] where

378   the inhibiting effect of the YSZ skeleton on Ni coarsening at typical SOC operating temperature was pointed

379   out. The homogenization of microstructural parameters as observed here after one year of electrolysis operation

380   leads to the tentative conclusion that the different conditions experienced by the cell at the two extremities are

381   more important in the first hundreds of hours of cell life. On the other hand, different percolation degrees

382   through the Ni phase were observed at the two extremities of the cell after the long-term testing showing, when

383   using this parameter, the most severe change to the Ni network at the inlet where the cell is more polarized.

384   All the microstructural features investigated in this study pointed out significant degradation both at the inlet

385   and the outlet of the tested cell that was used in a 25-cell stack compared to the non-tested reference cell.

386   Moreover, the degree of degradation of the two locations analyzed in the tested cell shows similar trends and

387   only some microstructural parameters (e.g. TPB length) indicate significant difference between the inlet and

388   the outlet side of the tested cell. Several studies proved that the Ni particle size increases mainly in the first

389   thousands of hours of testing [28, 43-45] and only small modification can be detected afterwards. After 1 year

390   of operation, as it is the case in the current study, the coarsening rate of Ni in the electrode is supposed to be

391   slow. This would explain the almost identical Ni PSD at the inlet and the outlet side of the long-term tested

392   cell shown in Figure 5. Moreover, the local testing conditions between inlet and outlet will make the

393   degradation occurring first at the inlet side and with the time also at the outlet. Ni rearrangement dictates

394   changes in porosity and therefore a significant difference in pore size between the reference and the tested cell

395   can be detected, however the size of the pores computed on the tested cell is almost unchanged between the

396   two locations analyzed. A number of tests under the same operating conditions (temperature, current density,

397   polarization, and gas composition) but for different time duration have been run in order to investigate

398   intermediate stage of degradation. The Ni/YSZ electrode microstructure is currently being characterized and

399   the results will be reported elsewhere.

400   The results for the characteristic pathway diameter illustrated in Figure 7 highlight a significant reduction in

401   percolation through the nickel phase, the total amount of pathways percolated throughout the volume (i.e.

402   percolating TPB sites) decreases strongly. Nevertheless, the diameters of the pathways that remain percolated

403   shows a mild increase. This could be the effect of a microstructural degradation driven by curvature

404   minimization. The effect of this process will lead to the disconnection of pathways connected through small

405   bottlenecks while a more stable behavior during operation will be observed for wider pathways characterized

406   by low curvature resulting in an overall decrease in percolation but an increase of the characteristic pathway

407   diameter for the remaining Ni pathways. De Angelis et al. [46] used x-ray tomography for investigating

408   Ni/YSZ cermets evolution. They observed that nickel coarsening leads to a loss of nickel connectivity and an

409 improvement in connectivity through the pore phase. The reduced tortuosity for the pore phase reported in

410 Table 2 finds an explanation in the improved connectivity of the pores.

411 An additional effect of the coarsening process is the increase of particle size shown in Figure 5: smaller nickel

412 particles are present in the reference cell after the reduction of NiO to Ni, these particles are characterized by

413 high curvature and disappear during the coarsening process in favor of bigger features with lower curvature.

414 TPB sites were quantified after segmentation for each of the three volumes analyzed and given in Table 2. The

415 lower percentage of percolated sites computed at the inlet side of the tested cell compared to the outlet is in

416 agreement with the observation reported by Mogensen et al. [39] and by Hauch et al. [8 (Cell A and B)] at the

417 cell level, Fang et al. [14] reported similar funding at the stack level . The inlet side is supposed to be exposed

418 to highest value of local current density which can contribute to a faster degradation. Chen et al. [38] simulated

419 the current density distribution in the cell in the direction of the steam flow for two cells with different oxygen

420 electrodes, the average current density of the two cells was ~ 0.9 and ~ 1.2 A/cm^2, respectively [38]. The

421 differences between inlet and outlet in current density were ~ 0.19 and ~ 0.35 A/cm^2, for the two cells

422 respectively. A rough estimation of the difference in current density between inlet and outlet for the cell

423 analyzed in the current study can be done considering that such a difference is approximately 20% of the

424 average value. Therefore, for the current case we can estimate the difference to be ~ 0.14 A/cm^2 resulting in ~

425 0.79 A/cm^2 at the inlet side and ~ 0.65 A/cm^2 at the outlet. Starting from 86 % of active TPB sites for the

426 reference cell only 62 % and 53 % were found at the outlet and the inlet of the tested cell, respectively. Knibbe

427 et al. [7] and Chen et al. [11] investigated the effect of the current density on the Ni/YSZ electrodes

428 microstructure. Ni coarsening and re-distribution were the main effects when the cells were tested at a current

429 density below -1 A/cm^2 (the cells were tested at 800 and 850 °C and an estimated fuel electrode polarization

430 of ~ 50 - 150 mV) [11]. For higher values of current density the formation of nanoparticles and impurities, and

431 the detachment of Ni from the YSZ scaffold were observed in the microstructures [7, 11]. These phenomena

432 contributed to the more pronounced performance degradation observed at higher current density [7, 11]. The

433 low current density used for the stack examined in the present study can explain the lack of nanoparticles at

434 the interfaces between Ni and YSZ as observed in [7] and [11] for higher value of current density and local

435   polarization. These percolating TPB results also fit well with the analysis of characteristic pathway diameter

436   and the tortuosity factor, which reveal that the one-year test has weakened transport properties of the Ni-

437   network: there is a loss in TPB percolation through the Ni phase and an increase in the tortuosity factor of the

438   Ni network for the conduction of electrons.

439   Not many studies focused on the quantification of SOEC microstructure parameters. Jørgensen and Bowen

440   [25] determined microstructural parameters for a single SOEC tested for approximately 1300 hours [25, 34]

441   where the same method for the calculation of TPB was implemented. In that specific case, 80 % of the TPB

442   was percolating after the testing. The higher percolation recorded in [25] could be due to several factors such

443   as shorter testing time, lower current density (- 0.5 A/cm^2) and therefore lower fuel electrode overpotential,

444   and also to the different gas composition used (50 % steam and 50 % H$_2$) versus the here used 90/10. More

445   details on the testing parameters can be found in [34]. A quantification of SOEC Ni/YSZ electrode

446   microstructure was performed also in [47] where the total TPB length was computed to be 4.63 µm/µm^3 with

447   3.07 µm/µm^3 of active sites in the commercial cell analyzed [48] versus the here reported 3.28 µm/µm^3 and

448   2.83 µm/µm^3.

449   Here, the reference cell could be compared only with one more step in time the full 9000 hours. However, a

450   previous study [39] has showed a difference in the rate of degradation of the percolation between the inlet and

451   the outlet side of the cell. After 128 hours the degradation is more marked at the inlet than at the outlet while

452   after 678 hours of test the difference started disappearing [39]. Similar results showing a faster degradation at

453   the inlet than at the outlet were also reported by Hauch et al. [8 (Cell A and B)]. Further, analyses of the

454   difference in degradation rate between inlet and outlet are currently underway.

455   The results presented in this work show that differences between the inlet and the outlet of the cell after long-

456   term testing could be detected only for some of microstructural parameters. TPB length illustrates recognizable

457   differences between the inlet and the outlet of the tested cell. The trend already reported in other studies [8

458   (Cell A and B), 14, 39] (i.e. lower degradation rate at the outlet side) was also observed here but only through

459   some of the features considered. Based on the results of the current and previous studies [29], we hypothesize

460   herein that the degradation of the investigated cell is connected to different local operating conditions

461 experienced at the two extremities. In particular, current distribution and gas composition are thought to play

462 an important role for the differences in degradation.

463 The characterization performed in this paper provides suitable input for microstructural modelling. The 3D

464 reconstruction of the reference cell could be used as input for the modelling and microstructural parameters

465 can be computed on the simulated geometries and linked to the experimental results presented in this work.

466 The investigation of the modelling results can provide information on the intermediate stages of the coarsening

467 process and related microstructural changes that cannot be detected and quantified during the operation of the

468 cell.

469

470 **Conclusion**

471 A detailed 3D microstructural characterization of a solid oxide electrolysis cell that was operated as part of a

472 stack for one year was performed, and microstructural parameters were compared with the results obtained on

473 a non operated reference cell manufactured as a part of the same batch of cells.

474 The depletion of Ni in the region close to the electrode-electrolyte interface (~ 5 µm) emerged both from the

475 EDS results and from the analysis of the three dimensional reconstructions. This effect was observed to occur

476 both at the inlet and at the outlet side of the cell after the long-term test in electrolysis mode. The same type of

477 analysis performed on the YSZ shows the stability of this phase during the cell aging.

478 The long-term test strongly affected the microstructure, starting from a reference cell with 86 % of percolating

479 sites, to 62 % at the outlet side and only 53 % at the inlet side after the test. Moreover, the shift towards larger

480 particles size together with the decrease of TPBs percolation and the increase of the tortuosity factor of the

481 nickel show a strong degradation in the network-quality of the three interpenetrating phases in the cermet. This

482 fact is likely responsible for the majority of the resistance increase observed over the one year aging: a

483 resistance increase (ASR) of ~ 42 % was observed over 9000 hours test. [31].

484   Interestingly, the two locations investigated on the tested cell (i.e. inlet and outlet side) showed similar

485   characteristics in microstructural changes/degradation, slightly more pronounced at the inlet. The higher loss

486   of percolating TPB at the inlet side is likely due to the more harsh operating conditions experienced here:

487   larger current density (stronger polarization) and more moist gas composition.

488

489

495

496

Bibliography

1. P. Taylor, A. Smith, A. S. Pedersen, "Fuel Cells", *Encyclopedia of Environmental Management Fuel Cells*, 37–41 (2014), doi:10.1081/E-EEM-120050576

2. P. Taylor, A. Smith, A. S. Pedersen, "Electrolysis", *Encyclopedia of Environmental Management Fuel Cells*, 37–41 (2014), doi:10.1081/E-EEM-120050577

3. L. Becero, "Recent advances in high temperature electrolysis using solid oxide fuel cells : A review", *J. Power Sources* **203**, 4–16 (2012).

4. S. D. Ebbesen, J. S. Højgaard, A. Hauch, and M. B. Mogensen, "High Temperature Electrolysis in Alkaline Cells, Solid Proton Conducting Cells, and Solid Oxide Cells", *Chem. Rev.* **114**, 10697-10734 (2014).

5. D. S. Ebbesen, C. Graves, A. Hauch, S. H. Jensen, and M. B. Mogensen, "Poisoning of Solid Oxide Electrolysis Cells by Impurities", *J. Electrochem. Soc.* **157**(10) B1419-B1429, (2010), doi:10.1149/1.3464804

6. Q. Fu, C. Mabilat, M. Zahid, A. Brisse, and L. Gautier, "Syngas production Via high-temperature steam/CO2 co-electrolysis: an economic assessment", *H. O. T. Energy & Environmental Science* (2010), doi:10.1039/c0ee00092b

7. R. Knibbe, L. Traulsen, A. Hauch, S. D. Ebbesen, and M. B. Mogensen, "Solid Oxide Electrolysis Cells : Degradation at High Current Densities", *J. Electrochem. Soc.* **157**(8) B1209-B1217 (2010), doi:10.1149/1.3447752

8. A. Hauch, K. Brodersen, M. Chen, and M. B. Mogensen, "Ni / YSZ electrodes structures optimized for increased electrolysis performance and durability", *Solid State Ionics* **293**, 27–36 (2016).

9. J. Schefold, A. Brisse, and F. Tietz, "Nine Thousand Hours of Operation of a Solid Oxide Cell in Steam Electrolysis Mode", *J. Electrochem. Soc.* **159**(2), A137-A144 (2012)

10. F. Tietz, D. Sebold, A. Brisse, and J. Schefold, "Degradation phenomena in a solid oxide electrolysis cell after 9000 h of operation", *J. Power Sources* **223**, 129–135 (2013).

11. M. Chen, Y. L. Liu, J. J. Bentzen, W. Zhang, X. Sun, A. Hauch, Y. Tao, J. R. Bowen, and P. V. Hendriksen, "Microstructural Degradation of Ni / YSZ Electrodes in Solid Oxide Electrolysis Cells under High Current", *J. Electrochem. Soc.* **160**(8) F883-F891 (2013).

12. L. Holzer, B. Iwanschitz, T. Hocker, B. Münch, M. Prestat, D. Wiedenmann, U. Vogt, P. Holtappels, J. Sfeir, A. Mai, and T. Graule, "Microstructure degradation of cermet anodes for solid oxide fuel cells : Quantification of nickel grain growth in dry and in humid atmospheres", *J. Power Sources* **196**, 1279–1294 (2011).

13. A. Faes, D. Presvytes, C. G. Vayenas, and J. Van "Nickel – Zirconia Anode Degradation and Triple Phase Boundary Quantification from Microstructural Analysis", *Fuel Cells* **9**(6)*,* 841–851 (2009), doi:10.1002/fuce.200800147

530 14. Q. Fang, C. E. Frey, N. H. Menzler, and L. Blum. "Electrochemical Performance and Preliminary Post-
531 Mortem Analysis of a Solid Oxide Cell Stack with 20,000 h of Operation", *J. Electrochem. Soc.* **165**(2) F38-
532 F45 (2018).

533 15. C. Graves, Reversing and Repairing Microstructure Degradation in Solid Oxide Cells During Operation.
534 *ECS Tran.*, **57**(1) 3127-3136 (2013), 10.1149/05701.3127ecst

535 16. H. Yokokawa, H.Tu, B, Iwanschitz, and A. Maic, "Fundamental mechanisms limiting solid oxide fuel cell
536 durability", *J. Power Sources* **182**, 400–412 (2008).

537 17. D. Waldbillig, A. Woodb, and D.G. Ivey, "Electrochemical and microstructural characterization of the
538 redox tolerance of solid oxide fuel cell anodes", *J. Power Sources* **145**, 206–215 (2005).

539 18. Y.L. Liu, and C, Jiao, "Microstructure degradation of an anode/electrolyte interface in SOFC studied by
540 transmission electron microscopy", *Solid State Ionics* **176**, 435–442 (2005).

541 19. P. R. Shearing, J. Golbert, R. J. Chater, and N. P. Brandon, "3D reconstruction of SOFC anodes using a
542 focused ion beam lift-out technique", *Chem. Eng. Sci.* **64**, 3928–3933 (2009).

543 20. H. Iwai, N. Shikazono, T. Matsui, H. Teshima, and M. Kishimoto, "Quantification of SOFC anode
544 microstructure based on dual beam FIB-SEM technique", *J. Power Sources* **195**, 955–961 (2010).

545 21. J. R. Wilson, M. Gameiro, K. Mischaikow, W. Kalies, P. W. Voorhees, and S. A. Barnett, "Three-
546 Dimensional Analysis of Solid Oxide Fuel Cell Ni-YSZ Anode Interconnectivity". *Microsc. Microanal*. **15**,
547 71–77 (2017).

548 22. P. S. Jørgensen, S. L. Ebbehøj, and A. Hauch, "Triple phase boundary specific pathway analysis for
549 quantitative characterization of solid oxide cell electrode microstructure Publication date : Triple phase
550 boundary specific pathway analysis for quantitative characterization of solid oxide cell electrode", *J. Power*
551 *Sources* **279**, 686–693 (2015).

552 23. T. Shimura, Z. Jiao, S. Hara, and N. Shikazono, "Quantitative analysis of solid oxide fuel cell anode
553 microstructure change during redox cycles", *J. Power Sources* **267**, 58–68 (2014).

554 24. P. S. Jørgensen, K. V. Hansen, R. Larsen, and J. R. Bowen, "Geometrical characterization of interconnected
555 phase networks", *Journal Microsc.* **244**, 45–58 (2011).

556 25. P. S. Jørgensen, and J. R. Bowen, "Determination of Three Dimensional Microstructure Parameters from
557 a Solid Oxide Ni/YSZ Electrode after Electrolysis Operation", *ECS Tran.* **35**(1), 1655-1660 (2011),
558 10.1149/1.3570152

559 26. B. Münch, and L. Holzer, "Contradicting Geometrical Concepts in Pore Size Analysis Attained with
560 Electron Microscopy and Mercury Intrusion", *J. Am. Ceram. Soc.* **91** (12) 4059–4067, (2008).

561 27. P. Hjalmarsson, X. Sun, Y.-L. Liu, and M. Chen, "Durability of high performance Nieyttria stabilized
562 zirconia supported solid oxide electrolysis cells at high current density", *J. Power Sources* **262**, 316-322
563 (2014).

28. P. Tanasini, M. Cannarozzo, P. Costamagna, A. Faes, J. Van Herle, A. Hessler-Wyser, and C. Comninellis, "Experimental and Theoretical Investigation of Degradation Mechanisms by Particle Coarsening in SOFC Electrodes", *Fuel Cells* **9**(5), 740–752 (2009), doi:10.1002/fuce.200800192

29. M. Trini, P. S. Jørgensen, A. Hauch, M. Chen, P. V. Hendriksen, "Microstructural Characterization of Ni/YSZ Electrodes in a Solid Oxide Electrolysis Stack Tested for 9000 Hours", *ECS Tran.* **78** (1), 3049-3064 (2017), 10.1149/07801.3049ecst

30. G. Rinaldi, S. Diethelm, E.Oveisi, P. Burdet, J. V. Herle, D. Montinaro, Q. Fu, and A. Brisse, "Post-test Analysis on a Solid Oxide Cell Stack Operated for 10,700 Hours in Steam Electrolysis Mode", *Fuel Cells* **17**(4), 541–549 (2017).

31. A. Brisse, J. Schefold, G. Corre, and Q. Fu, "Performance and Lifetime of Solid Oxide Electrolyzer Cells and Stacks", *11th European SOFC & SOE Forum,* **B1405** 48–59 (2014).

32. P. S. Jørgensen, S. L. Ebbehøj, and A. Hauch, "Triple phase boundary specific pathway analysis for quantitative characterization of solid oxide cell electrode microstructure", *J. Power Sources* **279**, 686-693 (2015), doi: 10.1016/j.jpowsour.2015.01.054

33. S. J. Cooper, A. Bertei, P. R. Shearing, J. A. Kilner, and N. P. Brandon, "ScienceDirect TauFactor : An open-source application for calculating tortuosity factors from tomographic data". *SoftwareX* **5**, 203–210 (2016).

34. A. Hauch, S. D. Ebbesen, S. H. Jensen, and M. B. Mogensen, "Solid Oxide Electrolysis Cells: Microstructure and Degradation of the Ni/Yttria-Stabilized Zirconia Electrode", *J. Electrochem. Soc.,* **155**(11), B1184-B1193 (2008).

35. P. S. Jørgensen, K. Yakal-kremski, J. Wilson, J. R. Bowen, and S. Barnett, "On the accuracy of triple phase boundary lengths calculated from tomographic image data", *J. Power Sources* **261**, 198–205 (2014).

36. W. M. Harris, and W. K.S. Chiu, "Determining the representative volume element size for three-dimensional microstructural material characterization. Part 1: Predictive models", *J. Power Sources* **282**, 552–561 (2015).

37. J. J. Lombardo, R.A. Ristau, W. M. Harris, and W. K. S. Chiu, "Focused ion beam preparation of samples for X-ray nanotomography", J. Synchrotron Radiat **19**, 789-796 (2012).

38. M. Chen, X. Sun, C. Chatzichristodoulou, S. Koch, P. V. Hendriksen, and M. B. Mogensen, "Thermoneutral Operation of Solid Oxide Electrolysis Cells in Potentiostatic Mode", *ECS Trans.* **78**(1) 3077-3088 (2017).

39. M. B. Mogensen, A. Hauch, X. Sun, M. Chen, Y. Tao, S. D. Ebbesen, K. V. Hansen, and P. V. Hendriksen, "Relation Between Ni Particle Shape Change and Ni Migration in Ni–YSZ Electrodes – a Hypothesis", *Fuel Cells* **17**(4), 434–441 (2017).

40. M.H. Pihlatie, A. Kaiser, M. Mogensen, and M. Chen, "Electrical conductivity of Ni–YSZ composites: Degradation due to Ni particle growth", *Solid State Ionics* **189**, 82–90 (2011).

41. Z. Jiao, and N. Shikazono, "Study on the effects of polarization on local morphological change of nickel at active three-phase-boundary using patterned nickel-film electrode in solid oxide fuel cell anode", *Acta. Mater.* **135**, 124-131 (2017).

601   42. M. Hubert, J. Laurencin, P. Cloetens, B. Morel, D. Montinaro, and F. Lefebvre-Joud, "Impact of Nickel
602   agglomeration on Solid Oxide Cell operated in fuel cell and electrolysis modes" , *J. Power Sources* **397**, 240-251
603   (2018).

604   43. R. Vaßen, D. Simwonis, and D. Stover, "Modelling of the agglomeration of Ni-particles in anodes of solid
605   oxide fuel cells", *J. Mater. Sci.* **36**, 147-151 (2001).

606   44. D. Simwonis, F. Tietz, D. Stover, "Nickel coarsening in annealed Ni / 8YSZ anode substrates for solid
607   oxide fuel cells", *Solid State Ionics* **132**, 241–251 (2000).

608   45. S. Gao, J. Li, and Z. Lin, "Theoretical model for surface diffusion driven Ni-particle agglomeration in
609   anode of solid oxide fuel cell". *J. Power Sources* **255**, 144–150 (2014).

610   46. S. De Angelis, P. S. Jørgensen, E. H. R. Tsai, M. Holler, K. Kreka, and J. R. Bowen, "Three dimensional
611   characterization of nickel coarsening in solid oxide cells via ex-situ ptychographic nano-tomography", *J.*
612   *Power Sources* **383**, 72–79 (2018).

613   47. F. Usseglio-Viretta, J. Laurencin, G. Delette, J. Villanova, P. Cloetens, and D. Leguillon, "Quantitative
614   microstructure characterization of a Ni e YSZ bi-layer coupled with simulated electrode polarisation", *J. Power*
615   *Sources* **256**, 394–403 (2014).

616   48. R. N. Basu, G. Blass, H. P. Buchkremer, D. Stöver, F. Tietz, E. Wessel, and I. C. Vinke, "Simplified
617   processing of anode-supported thin film planar solid oxide fuel cells", *J. Eur. Ceram. Soc.* **25**, 463–471 (2005)

618

619

620

621

622

623

624

625

626

627

628   Table 1: Parameters used for the 1-year stack test [31].

Period [hours]	Temperature [°C]	Steam conversion [%] (constant)	Air flow [Nl/min]	Steam[%]/ Hydrogen [%] feed		Hydrogen flow [Nl/min]	Current density [A/cm^2]	Degradation [%/1000 h]
				Inlet	Outlet			
0-2175	750	50	28	90/10	45/55 (calculated)	1.95	-0.57	2.0
2175-8700						2.45	-0.72	2.0*

629   *average value

630

631

632

633

634

635

636

637

638

639

640

641

642

643

644

645

646   Table 2: Phase fraction, total and percolating TPB and surface area calculated on 3D reconstructions of all the samples

647   for the three phases of interest. Based on cell manufacturing data, the volume ratio between Ni and YSZ can be expected

648   to be Ni/YSZ: 40/60 vol%.

	Reference	Inlet	Outlet
Ni [vol%]	30.16 ± 2.50	23.80 ± 2.50	28.37 ± 2.50
Pore [vol%]	24.66 ± 2.50	29.06 ± 2.50	28.95 ± 2.50
YSZ [vol%]	45.18 ± 2.50	47.15 ± 2.50	42.68 ± 2.50
Total TPB [$\mu m/\mu m^3$]	3.28 ± 0.10	1.44 ± 0.10	1.67 ± 0.10
Percolating TPB [$\mu m/\mu m^3$]	2.83 ± 0.15	0.76 ± 0.15	1.04 ± 0.15
Percentage of Percolating TPB [%]	86.28 ± 3.41	52.84 ± 5.02	62.22 ± 4.53
Percentage of Percolating TPB Pore [%]	95.11 ± 10.00	93.22 ± 10.00	96.29 ± 10.00
Percentage of Percolating TPB YSZ[%]	98.89 ± 10.00	98.47 ± 10.00	98.86 ± 10.00
Percentage of Percolating TPB Ni[%]	91.60 ± 10.00	46.52 ± 10.00	42.96 ± 10.00
Pore surface area [$\mu m^2/\mu m^3$]	2.09 ± 0.05	1.72 ± 0.05	1.58 ± 0.05
YSZ surface area [$\mu m^2/\mu m^3$]	2.09 ± 0.03	2.07 ± 0.03	1.92 ± 0.03
Ni surface area [$\mu m^2/\mu m^3$]	1.74 ± 0.05	0.88 ± 0.05	1.05 ± 0.05
Pore/YSZ interface area [$\mu m^2/\mu m^3$]	1.22 ± 0.05	1.45 ± 0.05	1.23 ± 0.05
Pore/Ni interface area [$\mu m^2/\mu m^3$]	0.87 ± 0.05	0.27 ± 0.05	0.35 ± 0.05
YSZ/Ni interface area [$\mu m^2/\mu m^3$]	0.87 ± 0.05	0.62 ± 0.05	0.69 ± 0.05
Ni tortuosity factor direction 1	6.27 ± 2.00	50.50 ± 20.00	17.80 ± 20.00
Ni tortuosity factor direction 2	6.64 ± 2.00	13.70 ± 5.00	14.60 ± 5.00
Ni tortuosity factor direction 3	4.49 ± 2.00	26.40 ± 15.00	32.00 ± 15.00
Pore tortuosity factor direction 1	7.25 ± 2.00	3.69 ± 2.00	3.34 ± 2.00

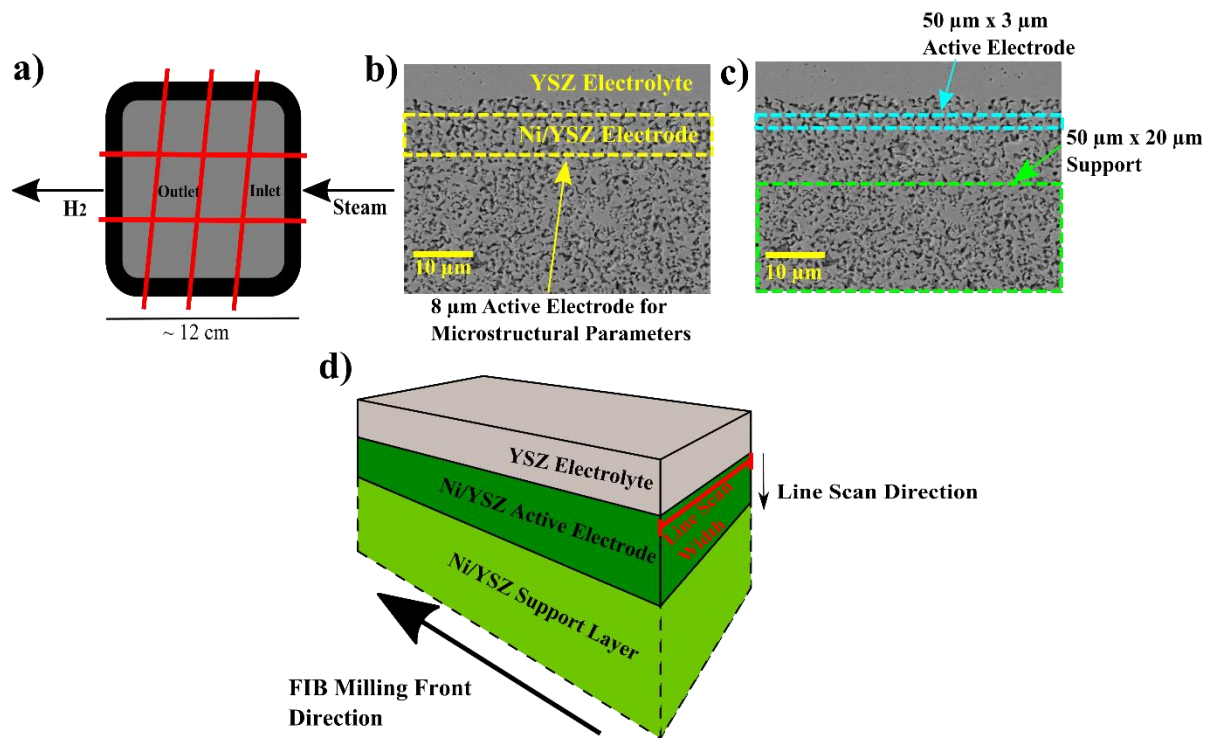|			
Pore tortuosity factor direction 2	5.78 ± 2.00	4.65 ± 2.00	5.01 ± 2.00
Pore tortuosity factor direction 3	5.37 ± 2.00	4.34 ± 2.00	4.00 ± 2.00

649

650

651

652

653

654

655

656

657

Figure 1: a) Schematic of stack top view showing the applied sectioning, the steam inlet and outlet are indicated in the picture together with the locations investigated through 3D reconstructions. b) SEM micrographs of the Ni/YSZ electrode of the reference cell highlighting innermost 8 µm of the active electrode analyzed in the microstructural characterization. c) Illustration of the regions for the EDS analysis in the support layer and close to the electrode-electrolyte interface. d) Schematic drawing of electrolyte ($\sim$ 5 µm), active fuel electrode ($\sim$ 15 µm), and part of the support layer (overall thickness $\sim$ 300 µm) illustrating the FIB milling front and line scan directions and the width of the line scan.

a)   b)   c)

~ 8 μm   ~ 8 μm   ~ 8 μm

Reference   Inlet   Outlet
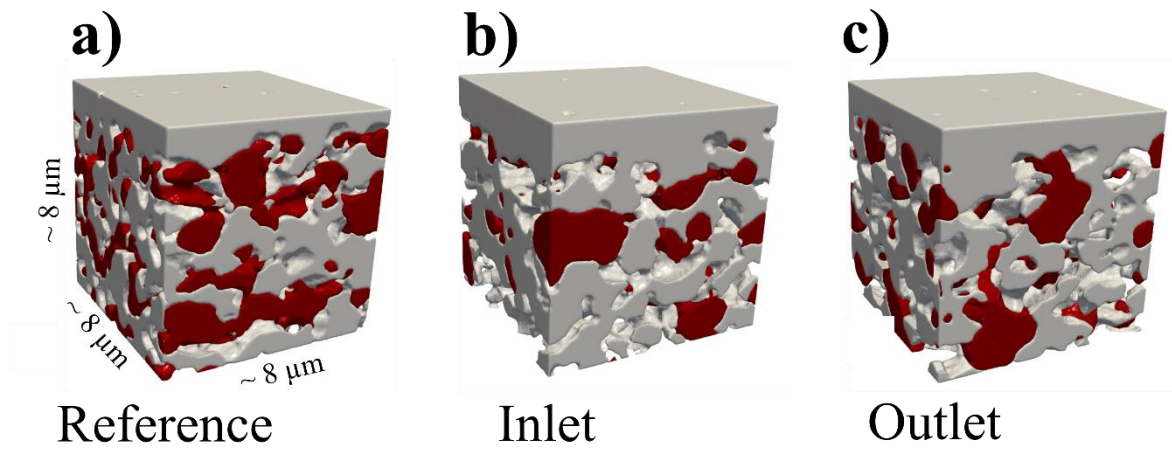
672

673   Figure 2: 3D reconstructions of sub-volumes extracted from: a) reference cell, b) inlet side of the tested cell c) outlet

674   side of the tested cell. Nickel is shown in red color, YSZ in gray and pores are transparent.

675

676

677

678

679

680

681

682
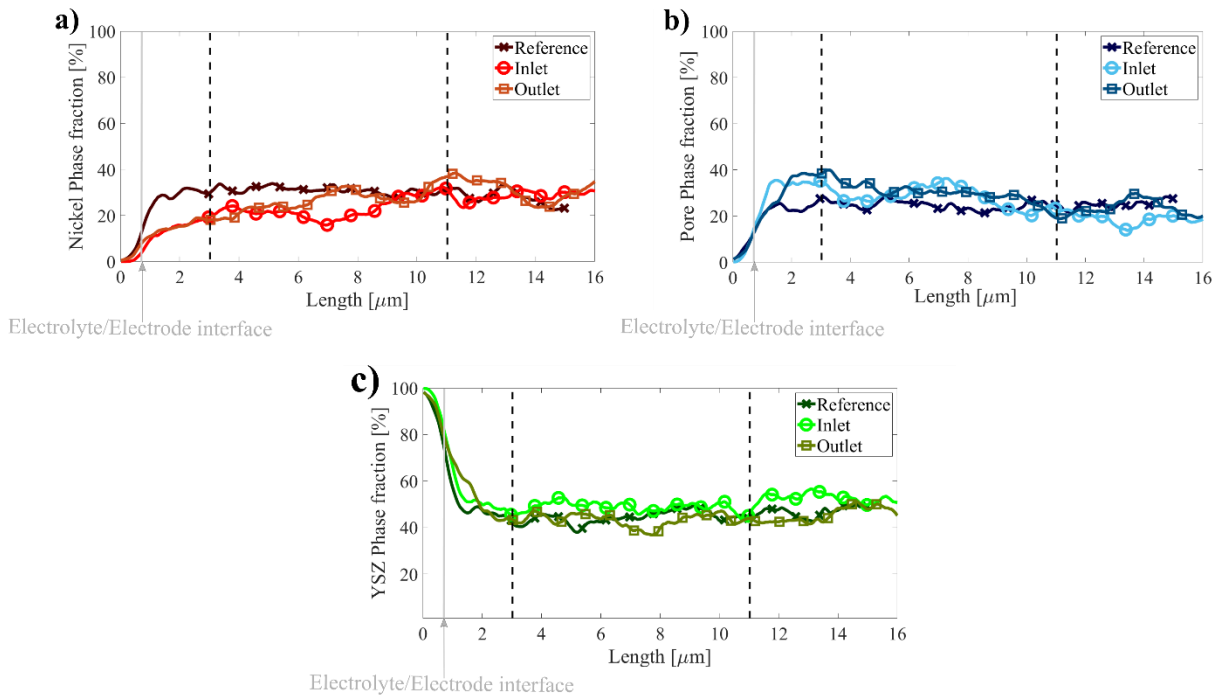
Figure 3: Phase fraction of the three phases form the FIB-SEM reconstructions in the direction perpendicular to the electrode-electrolyte interface: a) Ni, b) pores and c) YSZ. Each graph shows results for the reference cell and the tested cell at the inlet and the outlet.
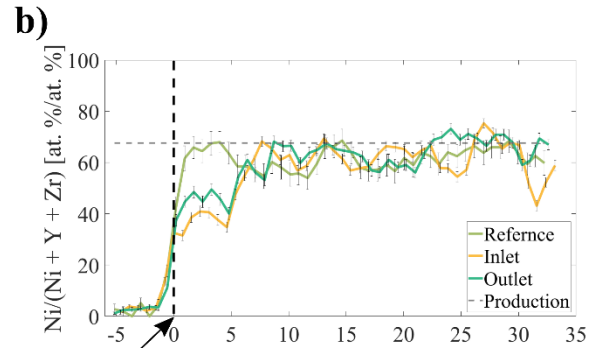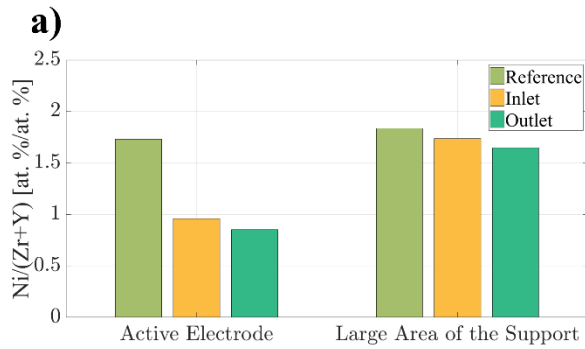
Figure 4: a) Ni/(Zr + Y) (atomic ratio) mean value in two regions of the fuel electrode: close to the electrode-electrolyte interface (average of EDS results computed on 25 x 3 µm^2 and 50 x 3 µm^2 areas) and on a large area of the support. b) Ni/(Ni + Y + Zr) (atomic ration) as a function of the distance from the electrolyte (EDS data obtained from 25 x (3 to 20) µm^2 and 50 x (3 to 10) µm^2 areas), the theoretical atomic ratio from the production is ~ 67 % and it is illustrated by a dashed gray line. The results are shown for the three sample analyzed in this study: reference, inlet and outlet.
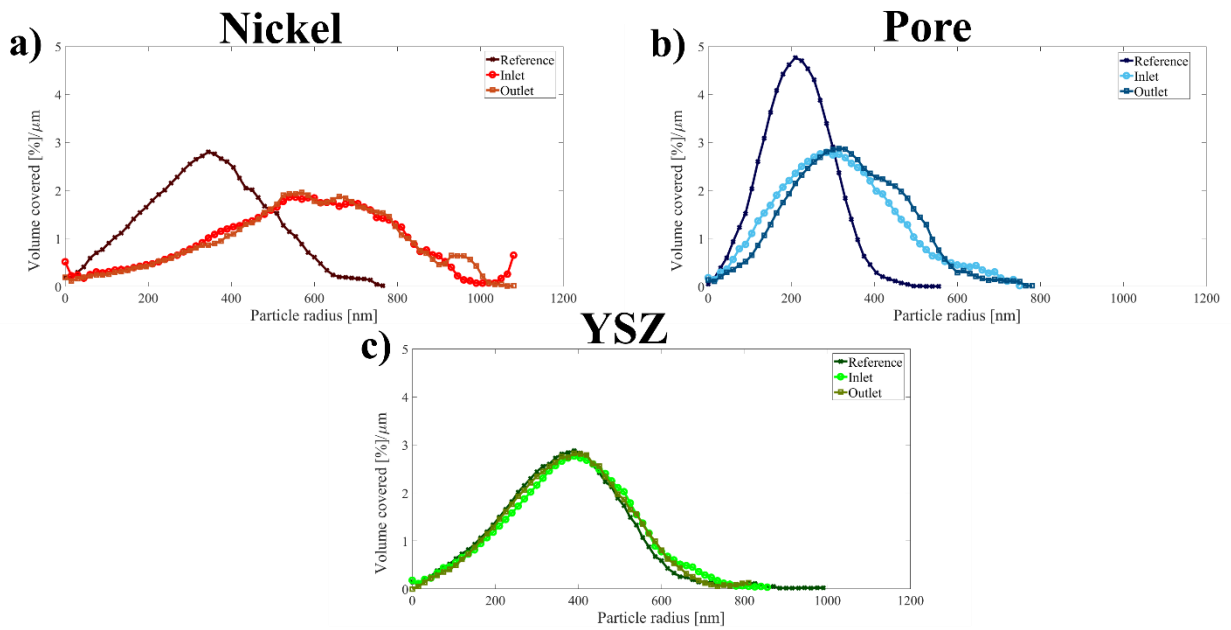
Figure 5: Continuous particles size distribution computed on the three volumes analyzed, each line in the graphs refers to one of the three samples analyzed: reference cell and aged cell at the inlet and the outlet side. Graph a) shows Ni PSD, graph b) the PSD of pores and graph c) the YSZ PSD.
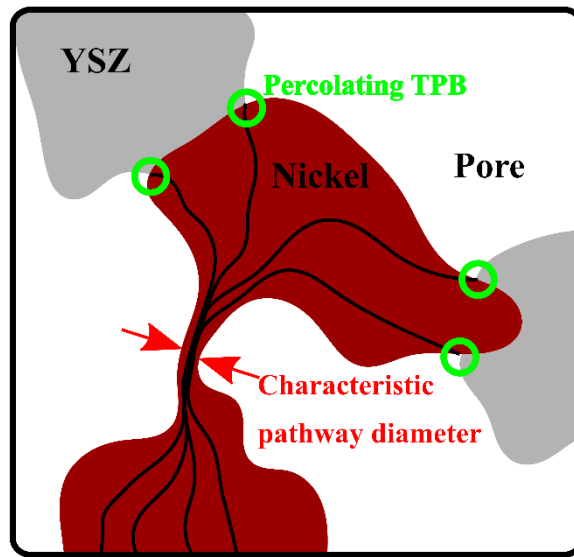
726

Figure 6: Sketch of characteristic pathway diameter concept. In the drawing, red arrows highlight the characteristic

pathway for the Ni phase, and percolating TPB between Ni (red), YSZ (gray) and pore (transparent) are circled in
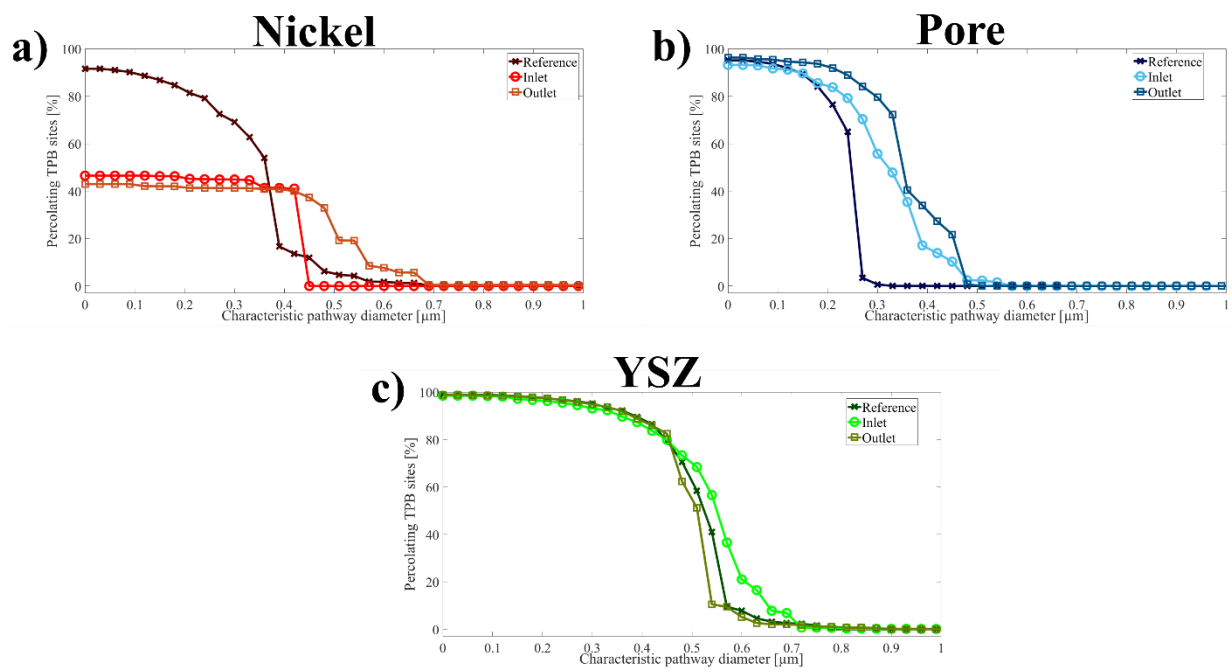
green.

730

731

732

733

734

735

736

737

738

739

Figure 7: Characteristic pathway diameter calculated for each of the three phases of the electrode: a) Ni, b) Pore and c) YSZ. The three lines in each graph represent the reference cell and the tested one at the inlet and the outlet side, respectively.